The International Journal of Advanced Manufacturing Technology (2020) 107:2137–2149
https://doi.org/10.1007/s00170-020-05180-6

ORIGINAL ARTICLE

Influence of chisel edge axial rake angle on the drilling performance of helical point micro-drill

Zhiqiang Liang[1] · Haixin Guo[2] · Xibin Wang[1] · Yue Ma[2] · Tianfeng Zhou[1] · Xiaofei Sun[3] · Likun Jiang[3]

Received: 18 April 2019 / Accepted: 6 March 2020 / Published online: 14 March 2020

Abstract

The chisel-edge axial rake angle has an important effect on the processing performance of helical point micro-drills. In this research, the mathematical modeling for the spiral groove, helical flank, and cross-shaped chisel edge are conducted, and then three types of helical point micro-drills, each having a thinned chisel edge with an unequal axial rake angle, are designed and fabricated. Then, the finite element simulations and processing experiments of micro-drilling are performed separately, and the thrust force, torque, chip morphology, tool wear, and micro-hole machining quality are measured and evaluated. With the rise of the axial rake angle of the chisel edge, the curling degree of the chips and the thrust force were found to decrease owing to the increase of the rake angle along the inner cutting edge. The angle between the tool axis and chip axis was found to gradually decrease due to the reduction of the rake angle gradient along the cutting edge. Additionally, the thickness and width of the uncut chip of the inner cutting edge were found to increase, bringing about the rise in the torque. The wear degree of the micro-drills with a 0° axial rake angle (Type II) was the smallest due to their medium thrust force and torque, and a better micro-hole entrance morphology and minimum roundness were obtained. When drilling to the 30th hole, compared with the micro-drills with a − 10° axial rake angle (Type I) and 10° axial rake angle (Type III), the chisel edge maximum wear width of Type II ($\delta = 0°$) was respectively reduced by 82.43% and 19.69%, and the micro-hole roundness respectively decreased by 26.7% and 11.33%. The thrust force of Type I ($\delta = -10°$) was the largest, so it caused greater tool wear and poorer micro-hole quality. The larger torque and lower rigidity of the inner cutting edge of Type III ($\delta = 10°$) led to poorer drilling performance. Thus, helical point micro-drills having the 0° chisel edge axial rake angle are suitable for drilling 304 austenitic stainless steel.

Keywords Axial rake angle · Chisel edge thinning · Simulation analysis · Drilling experiment · Drilling performance

1 Introduction

Micro-drills having a diameter within 0.5 mm have been extensively used in many applications including precision mechanical components and advanced electronic products, such as in the production of laser gyroscope, engine fuel injector, micro-instrument structure, and thick multilayer PCB (printed circuit boards) [1–3]. Most micro-hole

✉ Zhiqiang Liang
liangzhiqiang@bit.edu.cn

Haixin Guo
18811318020@163.com

Xibin Wang
cutting0@bit.edu.cn

Yue Ma
15546108005@163.com

Tianfeng Zhou
zhoutf@bit.edu.cn

Xiaofei Sun
2539363645@qq.com

Likun Jiang
616567652@qq.com

[1] Key Laboratory of Fundamental Science for Advanced Machining, Beijing Institute of Technology, Beijing 100081, People's Republic of China

[2] School of Mechanical Engineering, Beijing Institute of Technology, Beijing 100081, People's Republic of China

[3] Shanxi Diesel Engine Industry Co., Ltd., Datong, Shanxi 037036, People's Republic of China

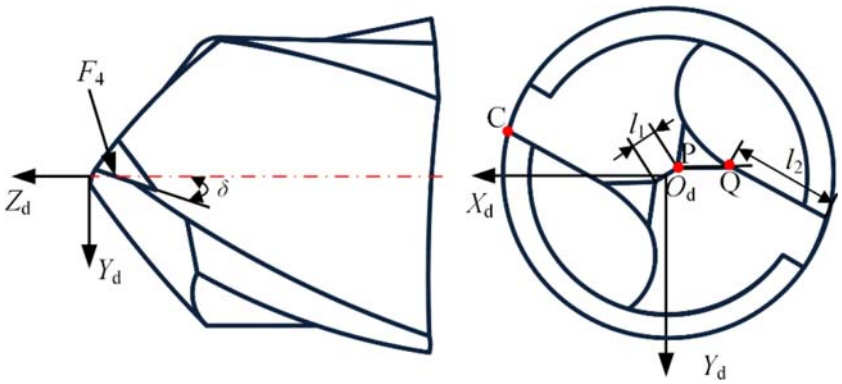

Fig. 1 The model of the thinned chisel edge

parts are made of difficult-to-machine materials including titanium alloy, superalloy, austenitic stainless steel, and so on. During the micro-hole drilling process, a large cutting force and serious size effect occur, and chip removal can be difficult, resulting in significant tool wear, fracture, and failure [4–6]. The machining precision is thus hard to be guaranteed.

Research shows that the machining performance of micro-drills can be improved noticeably via the method of chisel edge thinning. To discuss the influence of the length of the thinned chisel edge on micro-drilling performance, Guo et al. [7, 8] obtained a superior helical point micro-drill with a distinct chisel edge length via simulation analysis and drilling experiments. The optimized micro-drill displayed a satisfactory drilling performance compared to normal micro-drills. Nanbu et al. [9, 10] discussed the influence of the thinning of the axial rake angle on the drilling force, and found that the thinning of planar point micro-drills resulted in a reduction in drilling force. In terms of drill life, the optimum axial rake angle was in a range of − 10° to 0°. Xiang et al. [11] proposed an effective method of chisel edge regrinding for helical point micro-drills that make the angle distribution along the chisel edge more reasonable, then improves the machining performance of micro-drills. Wang et al. [12] utilized regular drill and thinned drill to process through-holes on PCB, and found that suitable chisel edge thinning can reduce the conglutination phenomenon of chips on the major flank and the flank wear of micro-drills. Lin et al. [13] proposed an accurate fabrication method of twist drills via thinning based on the position and direction of the abrasive wheel. The drilling experiment demonstrated that chisel edge thinning can improve the phenomenon of large negative rake angle distribution along the cutting edge and chisel edge.

As the diameter of the micro-drill is gradually reduced, the design and thinning of the chisel edge are more difficult. At present, there is little theoretical guidance for the chisel edge thinning of micro-drills. Some researchers have put forward a helical point micro-drill, and it has been confirmed that this drill exhibits better drilling performance than planar and conical point drills [14, 15]. However, few detailed investigations have been conducted concerning the influence of the axial rake angle on helical point micro-drills having thinned chisel edge.

Finite element simulation technique is a mathematical method for simulating real physical systems and uses finite unknowns to approximate an infinite unknown real system [16, 17]. DEFORM 3D, a commercial implicit finite element software, is widely applied in the machining field [18–20]. Thus, in the present research, the influence of the chisel edge axial rake angle on the drilling

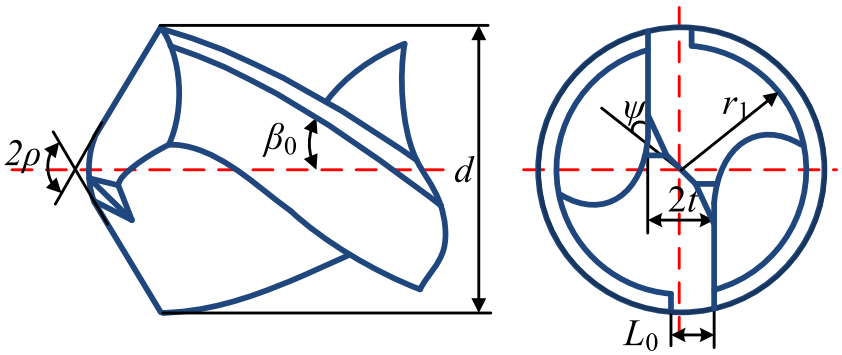

Fig. 2 Micro-drill geometry structure

Table 1 Structure parameters of the micro-drill

Tool name	Type I	Type II	Type III
Axial rake angle δ (°)	− 10	0	10
Tool diameter d (mm)	0.5	Web thickness $2t$ (mm)	0.125
Point angle 2ρ (°)	118	Helix angle β_0 (°)	30
Margin width L_0 (mm)	75	Chisel edge angle ψ (°)	55
Clearance radius r_1 (mm)	0.2125	Chisel edge length l_1 (μm)	42
Main cutting edge length l_2(μm)	150		

performance of micro-drills was analyzed by finite element simulations and micro-drilling experiments. The 3D models of micro-drills were built based on UG software, and the DEFORM-3D was used to conduct the simulation analysis of the micro-drilling process. The micro-drills were sharpened by the CNC tool grinder, and micro-drilling experiments were conducted. The tool processing performance was evaluated according to the chip morphology, drilling force, drill bit wear, and micro-hole processing quality. A helical point micro-drill having an optimal axial rake angle achieved via thinning is determined by the research results.

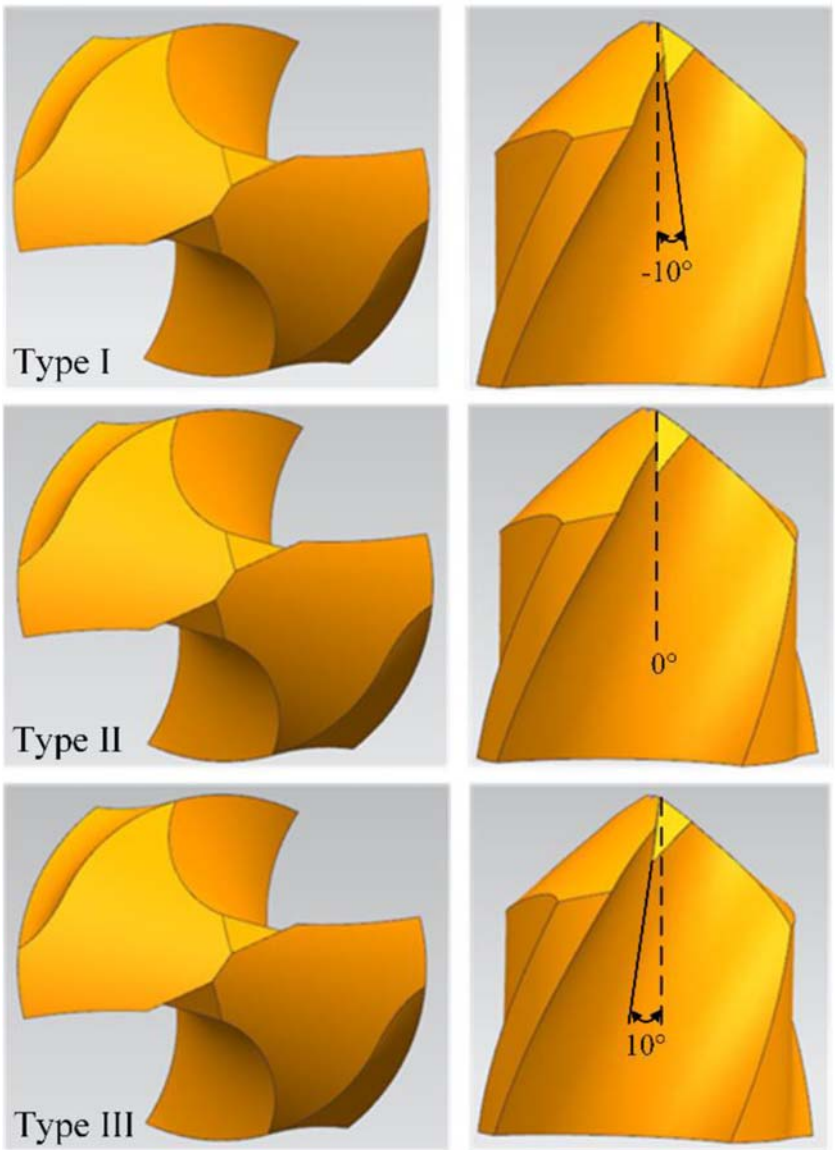

Fig. 3 Helical point micro-drills with unequal axial rake angles

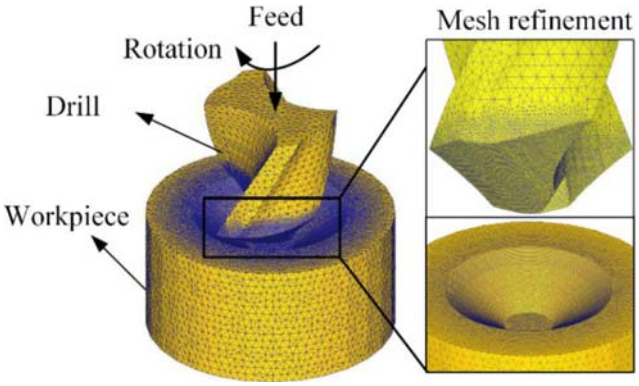

Fig. 4 Simulation model of the micro-drill and workpiece

2 Mathematical modeling for the helical point micro-drill

2.1 Mathematical modeling for the helical flank

According to the basic model put forward in Liang et al.'s work [21], the formula of the helical flank in the O_d-$X_dY_dZ_d$ system is determined as Eq. (1):

$$F_1 : Z_d\cos\phi - B\frac{\sin\phi}{\tan\theta} + X_a\sin\phi + \frac{\sqrt{[X_a\cos\phi - \sin\phi(Z_d + B)]^2 + {Y_a}^2}}{\tan\theta} + \frac{H}{2\pi}\arcsin\left(\frac{Y_a}{\sqrt{[X_a\cos\phi - \sin\phi(Z_a + B)]^2 + {Y_a}^2}}\right) = 0 \tag{1}$$

In the above equation, $X_a = X_d\cos\beta - Y_d\sin\beta$, $Y_a = Y_d\cos\beta + X_d\sin\beta$, and B, H, ϕ, θ, and β are the grinding parameters of the micro-drill flank. Thus, the mathematical equation of tool helical flank $F_2(X'_d, Y'_d, Z'_d) = 0$ will be accordingly acquired by plugging $X'_d = -X_d$, $Y'_d = -Y_d$, and $Z'_d = Z_d$ into Eq. (1).

2.2 Mathematical modeling for the spiral groove

The relative spiral movement between the parallel abrasive wheel and the tool generates the spiral groove of the micro-drill. When the abrasive wheel is fixed, the tool moves spirally along its axis, and the overlapping portion of the abrasive wheel and the tool movement track generates the micro-drill flute. In view of the spiral groove model established in Zhang et al.'s work [22], the cutting track can be obtained as follows:

$$R_m(u,\delta) = \begin{bmatrix} X_{Pm}(u,\delta) \\ Y_{Pm}(u,\delta) \end{bmatrix} = \begin{bmatrix} X_{Pf}\cos(-Z_{Pf}\tan(\beta_0)/r) - Y_{Pf}\sin(-Z_{Pf}\tan(\beta_0)/r) \\ X_{Pf}\sin(-Z_{Pf}\tan(\beta_0)/r) + Y_{Pf}\cos(-Z_{Pf}\tan(\beta_0)/r) \end{bmatrix} \tag{2}$$

$$R_f(u,\delta) = \begin{bmatrix} X_{Pf} \\ Y_{Pf} \\ Z_{Pf} \end{bmatrix} = \begin{bmatrix} R(u)\cos\delta + a_x \\ R(u)\sin\delta\cos\lambda - u\sin\lambda \\ R(u)\sin\delta\sin\lambda + u\cos\lambda \end{bmatrix} \tag{3}$$

Here, u and δ are defined as the position variables of any point N on the grinding wheel surface, r is the tool radius, β_0 is the helix angle, and a_x and λ are the position variables of abrasive wheel.

After calculating the numerical solution of the spiral groove profile, the equation of the flute section contour can be obtained via cubic spline interpolation. The micro-drill flute surface is produced by the spiral movement of the cross-section contour, and the spiral groove mathematical formula of the micro-drill can be written as:

$$F_3 : \begin{cases} X_d = w\cos v - f_H(w)\sin v \\ Y_d = w\sin v + f_H(w)\cos v \\ Z_d = z_c + rv/\tan\beta_0 \end{cases} \tag{4}$$

Here, w and v represent the shape variables to form the spiral groove surface, z_c stands for the z-coordinate value of the outer corner C in the O_d-$X_dY_dZ_d$ system.

2.3 Mathematical modeling for the thinned chisel edge

Since the chisel edge is produced by the intersecting line of the helical flank F_1 and F_2, the mathematical formula of the chisel edge L_0 in the O_d-$X_dY_dZ_d$ system can be derived by the simultaneous use of the equations of F_1 and F_2.

$$L_0 : 2X_a\sin\phi + \frac{\sqrt{[X_a\cos\phi - \sin\phi(Z_d + B)]^2 + {Y_a}^2} - \sqrt{[X_a\cos\phi + \sin\phi(Z_d + B)]^2 + {Y_a}^2}}{\tan\theta} + \frac{H}{2\pi}\left\{\arcsin\left(\frac{Y_a}{\sqrt{[X_a\cos\phi - \sin\phi(Z_d + B)]^2 + {Y_a}^2}}\right) + \arcsin\left(\frac{Y_a}{\sqrt{[X_a\cos\phi + \sin\phi(Z_d + B)]^2 + {Y_a}^2}}\right)\right\} = 0 \tag{5}$$

Figure 1 shows the model of the cross-shaped chisel edge. The rake face F_4, which is a plane, intersects with the chisel edge and the main lip at point P (x_p, y_p, z_p) and point Q (x_q, y_q, z_q), respectively, and the inner cutting edge PQ is then generated. With proper web thinning, the correct chisel edge length l_1 and main cutting edge length l_2 can be determined. The axial rake angle δ of the chisel edge stands for the angle between the rake face F_4 and the drill center axis. The

Table 2 Simulation parameters of micro-drilling

Parameters	Values
Feed rate	0.02 mm/r
Rotational speed	14,000 r/min
Drill material	Carbide containing 15% cobalt
Workpiece	AISI 304
Friction type	Shear
Friction value	0.7
Heat transfer coefficient	45
Separation	Cockcroft-Latham

mathematical equation of the rank face $F_4(X_d, Y_d, Z_d) = 0$ derived using Eq. (4) is expressed as follows:

$$F_4 : aX_d + bY_d + cZ_d + d = 0 \tag{6}$$

Here, the coefficients a, b, c, and d are decided by δ, l_1, and l_2.

3 Simulation analysis of the micro-drilling process

3.1 3D modeling for the helical point micro-drills with unequal axial rake angles

To analyze the influence of the axial rake angle on the micro-drills having thinned chisel edges, three types of helical point micro-drills were designed, each of which has a thinned chisel edge with an unequal axial rake angle. The tool structure parameters are presented in Fig. 2 and Table 1, respectively.

As presented in Fig. 3, the tool geometric models were built with UG software. Based on the DEFORM-3D software, the simulation model of micro-drilling was established and the simulation analysis of the drilling process was completed, as presented in Fig. 4. To improve the efficiency of finite element simulation, a conical concave surface was set on the upper surface of the workpiece model, so that the cutting edges of the drill model can quickly participate in cutting during the drilling simulation process. The meshes of the drill tip and the workpiece to be cut were refined, and the specific micro-drilling parameters in the simulation process were set according to Table 2.

3.2 Chip morphology

Figures 5 and 6 respectively present the simulation results of the chip morphologies produced by Type I ($\delta = -10°$), Type II ($\delta = 0°$), and Type III ($\delta = 10°$) when drilling to the hole depths of 0.03 mm and 0.06 mm. The chip curl phenomenon for each tool is obvious. When the drilling depth reaches 0.03 mm, the side-curl and up-curl degrees of the chips gradually decrease from Type I ($\delta = -10°$) to Type III ($\delta = 10°$) (see Fig. 5). When the micro-hole depth reaches 0.06 mm, the angle between the chip axis and tool axis gradually reduces from Type I ($\delta = -10°$) to Type III ($\delta = 10°$) (see Fig. 6).

In fact, both the chip flow direction and the gradient of the chip flow speed on the separation line between the chip and the tool have an effect on the side-curl of the chips. Among the cutting geometry parameters of micro-drills, the lip inclination angle λ_{se} and the rake angle γ_{oe} of the cutting edge are the

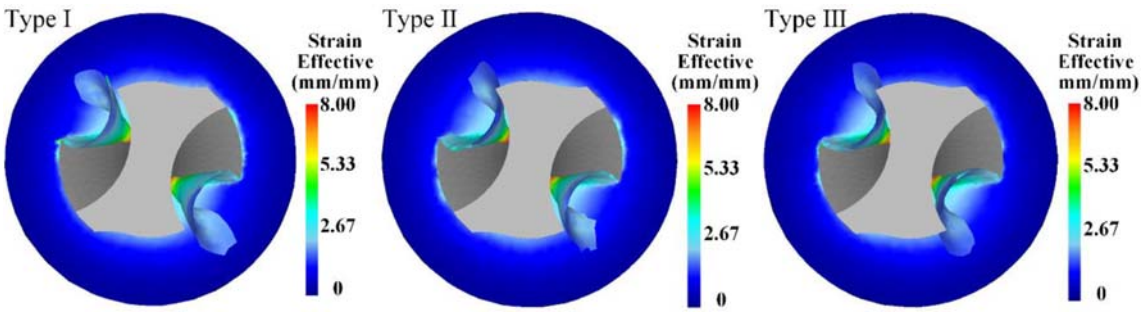

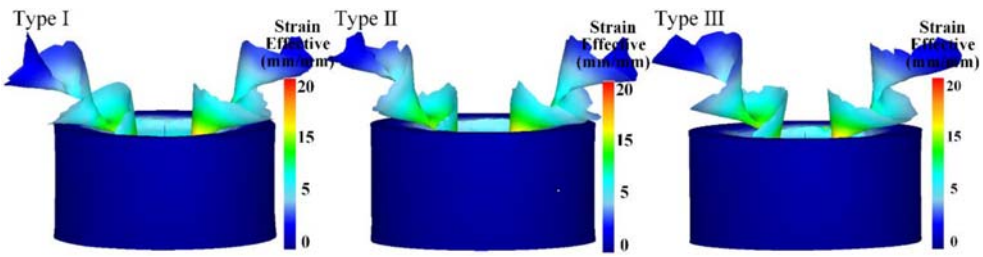

Fig. 6 Chip morphology of micro-drilling process when micro-hole depth is 0.06 mm

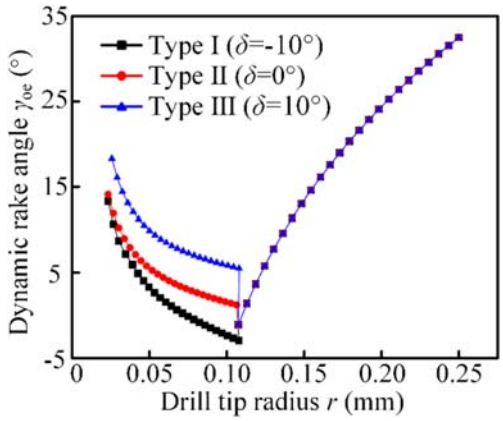

Fig. 7 Dynamic rake angle γ_{oe} changing with micro-drill radius

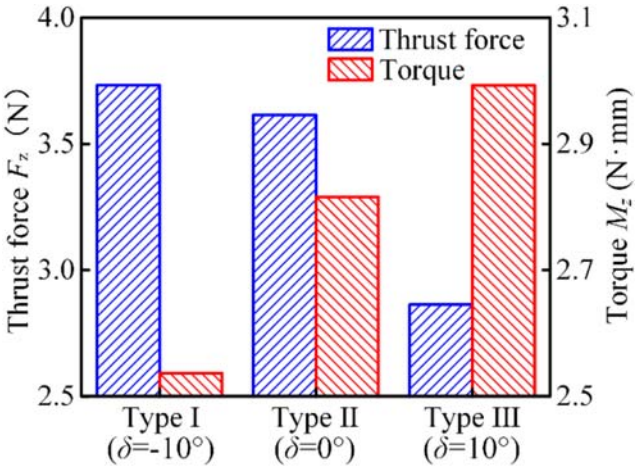

Fig. 9 Simulation results of drilling force

main factors affecting the flow and deformation of the chips. Since the start and end positions of the inner cutting edge of the three micro-drills are the same, their lip inclination angles are equal. Thus, only the rake angle is considered due to the equivalent lip inclination angle. The chip flow speed can be calculated based on the formula $v_{chip} = v_{cutting}/\Lambda_h$, where $v_{cutting}$ is the cutting speed and Λ_h is the chip deformation coefficient. In addition, the chip deformation coefficient Λ_h is calculated using the equation $\Lambda_h = \cos(\phi - \gamma_{oe})/\sin\phi$ and $\phi = \pi/4 - (\beta_f - \gamma_{oe})$, where ϕ stands for the shear angle and β_f represents the friction angle. Consequently, the rake angle γ_{oe} can make significant impacts on the chip deformation degree and chip flow velocity. A larger rake angle γ_{oe} results in a smaller chip deformation coefficient, ultimately leading to larger chip flow velocity. The rise in the change gradient of the rake angle creates a raise in the chip flow velocity gradient.

Referring to the calculation equation presented in Zhang et al.'s work [22], the value of the dynamic rake angle γ_{oe} changing with the tool radius under the condition of f = 0.02 mm/r is presented as Fig. 7, in which the drill tip radius stands for the distance between a point on the cutting edge and the drill center. The rake angle of inner cutting edge gradually raises from Type I ($\delta = -10°$) to Type III ($\delta = 10°$), resulting in a smaller chip deformation coefficient. Therefore, the deformation degree of the chips gradually decreases from Type I ($\delta = -10°$) to Type III ($\delta = 10°$). Figure 8 shows the simulation results of the chip flow velocity produced by Type I ($\delta = -10°$), Type II ($\delta = 0°$), and Type III ($\delta = 10°$) at the drilling depth of 0.03 mm. The rake angle gradient along the cutting edge gradually decreases from Type I ($\delta = -10°$) to Type III ($\delta = 10°$). The rake angles between inner turning point of inner cutting edge and outer turning point of main cutting edge for Type I ($\delta = -10°$) and Type III ($\delta = 10°$) are 19° and 14°, respectively, resulting in a reduction of chip flow speed gradient from Type I ($\delta = -10°$) to Type III ($\delta = 10°$). Therefore, the side-curl degree of the chips generated by Type I ($\delta = -10°$) is more obvious compared to that of Type II ($\delta = 0°$), and Type III ($\delta = 10°$). As the drilling depth increases, the chips flow toward the center of the micro-drills because of the serious side-curl phenomenon, and the chips are forced to up-curl when they are blocked by the drill web. With the intensification of the chip side-curl phenomenon, the degree of chip up-curl increases. The up-curl and side-curl degrees of the chips are gradually reduced from Type I ($\delta = -10°$) to Type III ($\delta = 10°$), so the chips flow more violently toward the center of the micro-drills. Therefore, the angle between the axes of the tool and chip is gradually reduced from Type I ($\delta = -10°$) to Type III ($\delta = 10°$).

Consequently, with the rise of the chisel edge axial rake angle, the side-curl and up-curl degrees of the chips gradually decreases, as do the angle between the axes of tool and chip.

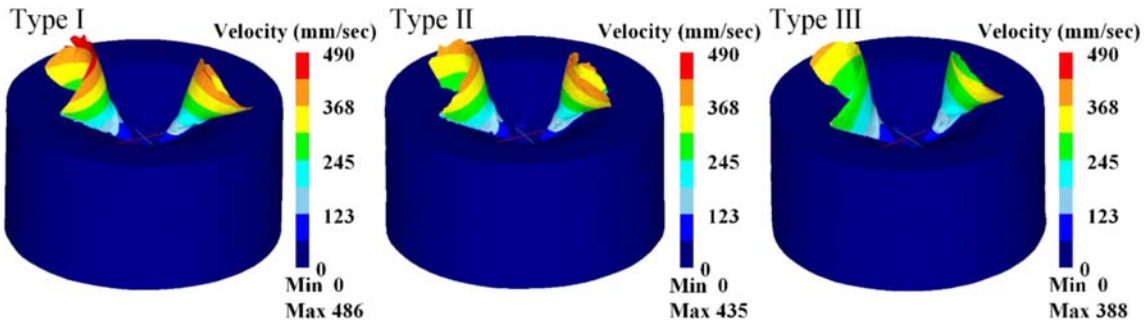

Fig. 8 Chip flow velocity of micro-drilling process when micro-hole depth is 0.03 mm

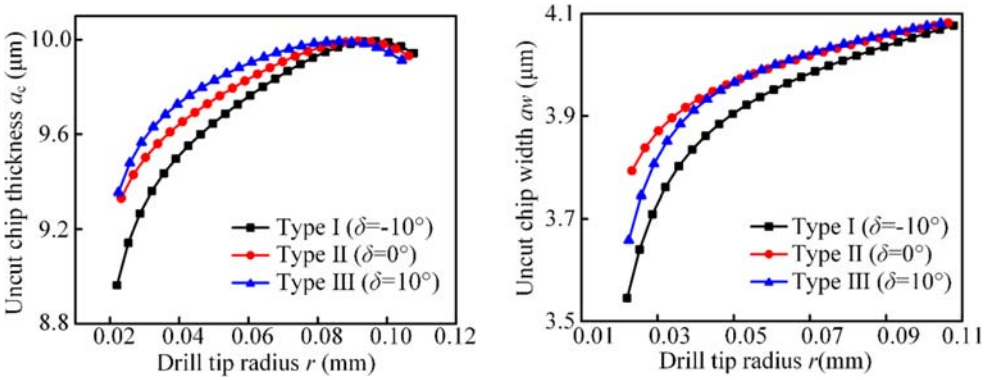

Fig. 10 Uncut chip thickness and uncut chip width changing with tool radius

Therefore, the chips will slide longer along the rake face, and the chips are prone to wrap around the drill body, which reduces the chip removal performance of the micro-drills and increases the friction between the rake face of the micro-drills and the chips.

3.3 Thrust force and torque

Figure 9 shows the average values of thrust force and torque in the drilling steady phase, and it is obvious that the thrust force gradually decreases from Type I ($\delta = -10°$) to Type III ($\delta = 10°$), while the torque rises from Type I ($\delta = -10°$) to Type III ($\delta = 10°$).

The axial rake angle of the thinned chisel edge affects the thrust force and torque by having obvious effects on the rake angle, thickness, and width of uncut chips. As the axial rake angle raises, the dynamic rake angle γ_{oe} along the inner cutting edge increases and chip deformation is reduced, leading to a decrease in the thrust force. Referring to the calculation method mentioned in Zhang et al.'s work [22], the calculated results of the thickness and width of uncut chips are presented in Fig. 10. With the rise of the axial rake angle, the thickness and width of the uncut chips of the inner cutting edge increase, bringing about an increase in the torque during the micro-drilling process. Furthermore, the angle between the tool axis and chip axis is gradually reduced from Type I ($\delta = -10°$) to Type III ($\delta = 10°$); thus, the chips slide along the micro-drill rake face over a long range, and the friction between the chip and micro-drill rake face increases. This also causes an increase of torque.

4 Fabrication of helical point micro-drills with unequal axial rake angles

The preparation of the helical point micro-drill with unequal axial rake angles was completed by the Makino Seiki six-axis CNC tool grinder, and the tool material is cemented carbide.

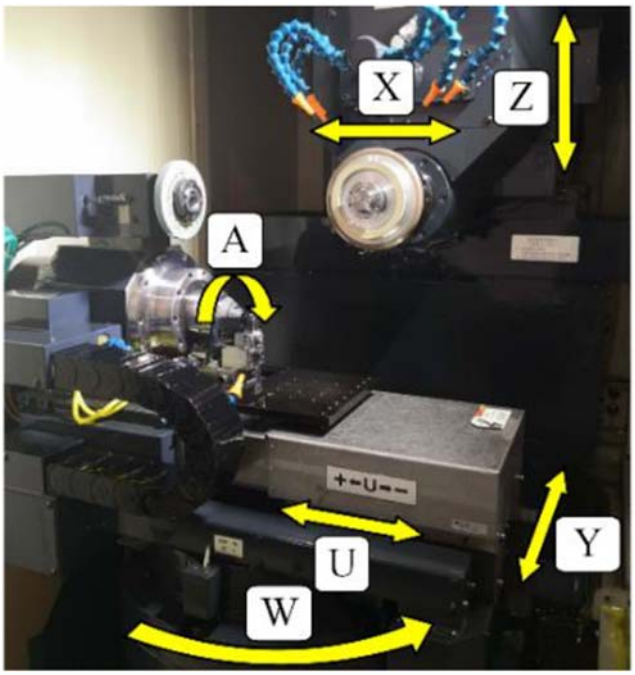

Fig. 11 Six-axis CNC grinding machine

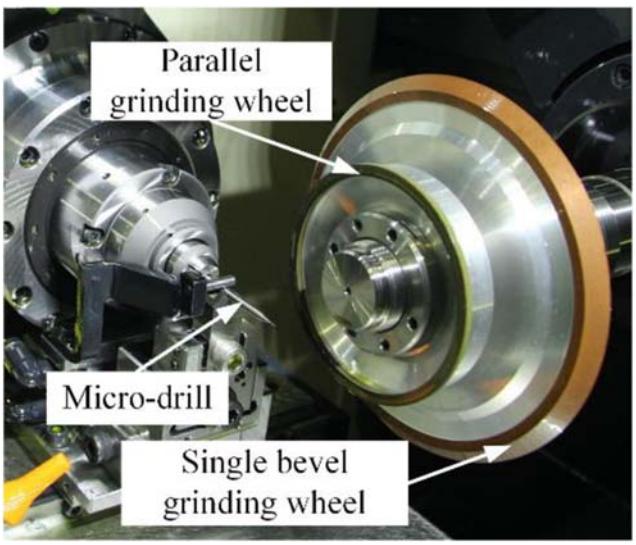

Fig. 12 Installation layout of the grinding wheels

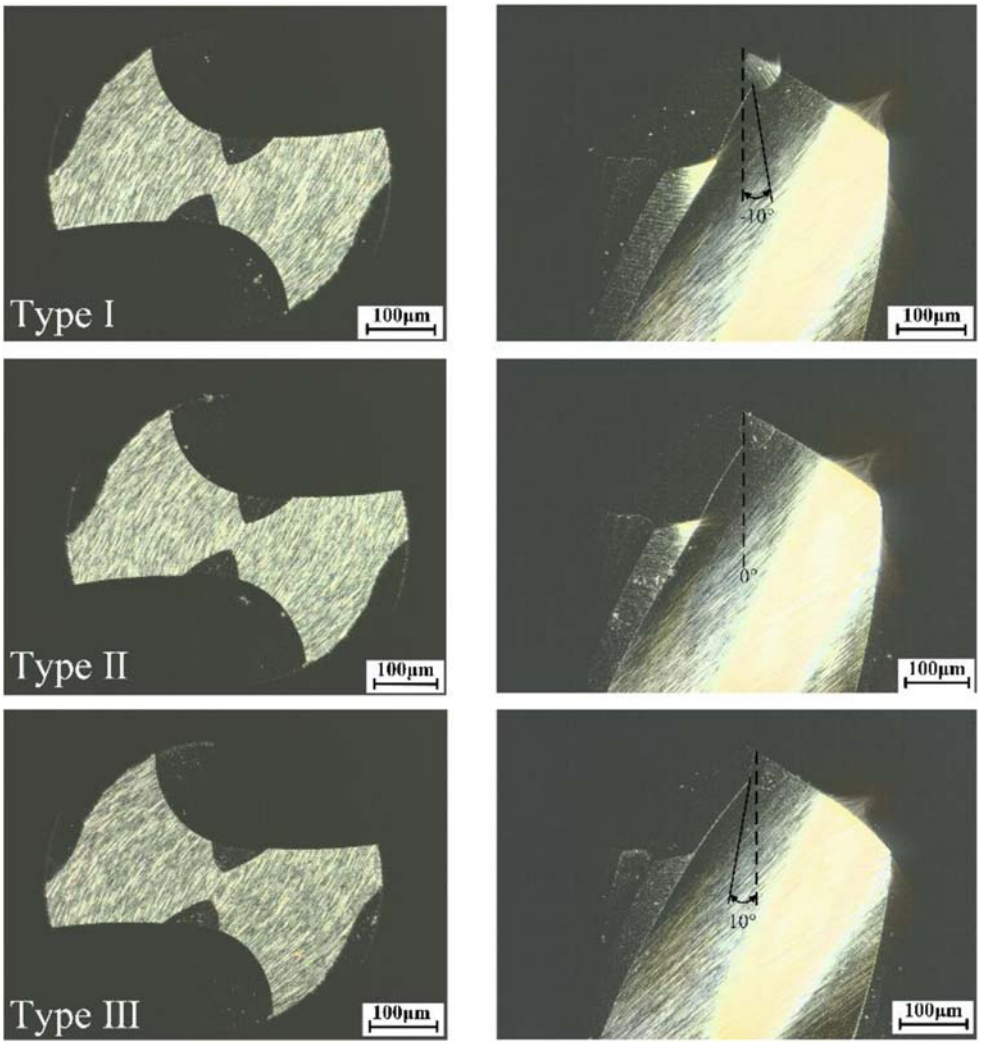

Fig. 13 Grinding experiment result of micro-drills having unequal axial rake angles

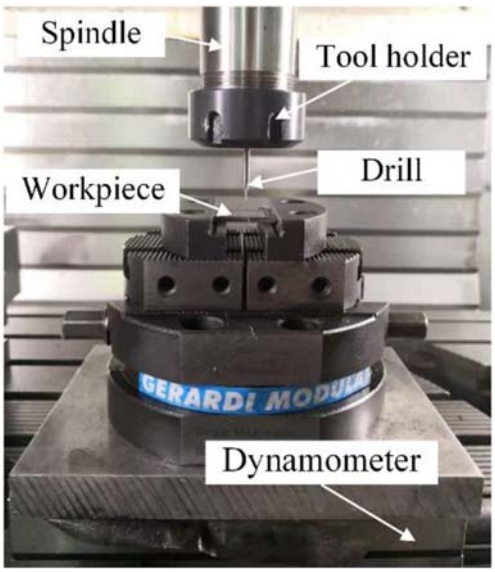

Fig. 14 Micro-drilling experiment setup

The configuration of the grinding machine and the movement of each axis is exhibited in Fig. 11, and Fig. 12 shows the installation layout of the grinding wheels for tool grinding. The grinding process of the helical flank is completed by the parallel grinding wheel, while the single bevel grinding wheel is used to grind the spiral groove and thinned chisel edge. Both of the above grinding wheels are diamond grinding wheel with the ceramic bond.

Table 3 Machining parameters for micro-drilling

Parameters	Values
Hole depth h	1 mm
Micro-hole diameter d	0.5 mm
Spindle speed n	14,000 r/min
Feed rate f	7, 14, 21, 28 mm/min
Cutting fluid type	Water-base cutting fluid
Workpiece material	304 austenitic stainless steel

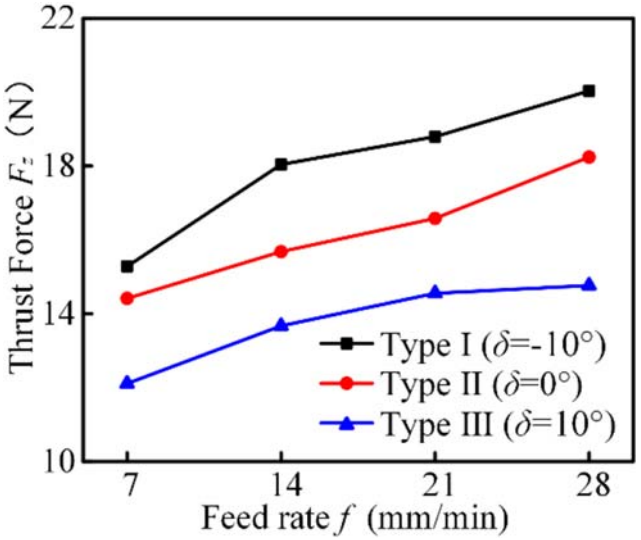

Fig. 15 Change of thrust force with the feed rate

Three types of helical point micro-drills having thinned chisel edge with different axial rake angles were respectively fabricated, and the results of the sharpened micro-drills are presented in Fig. 13. The drill flute length is 1.5 mm and the other tool geometry parameters are the same as those in Table 1.

5 Drilling performance of helical point micro-drills with unequal axial rake angles

As presented in Fig. 14, the micro-drilling experiments were completed by the DMG machining center to validate the processing performance of micro-drills with unequal axial rake angles. To obtain accurate experimental data, the drilling experiments were repeated three times. The Kistler piezoelectric dynamometer was used to measure the drilling force, and the mean value of thrust force during the stable drilling phase was acquired by DynoWare software. The tool wear status and processing quality of micro-holes were detected using the 3D laser scanning microscope, and the measurement results were analyzed and calculated by VK Analyzer software. The specific processing parameters used in the research are listed in Table 3.

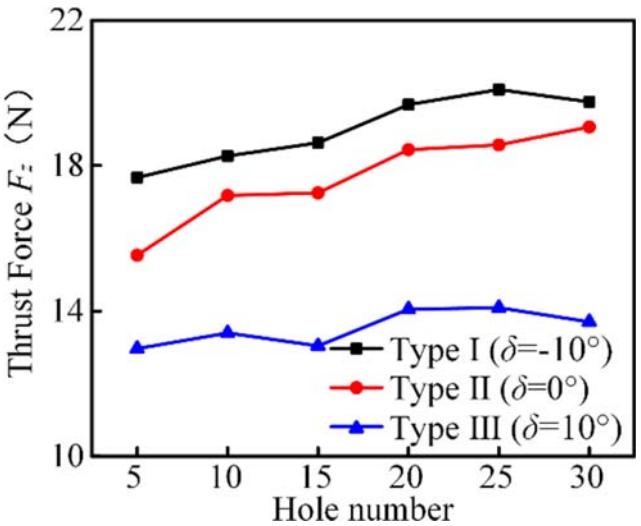

Fig. 16 Change of thrust force with the micro-hole number under feed rate f = 28 mm/min

5.1 Drilling force

Drilling experiments were conducted under respective feed rates of f = 7, 14, 21, and 28 mm/min, and Fig. 15 shows the mean drilling force during the stable drilling phase. Obviously, the thrust force is found to be positively related to feed speed. Under the condition of feed rate f = 28 mm/min, Type I ($\delta = -10°$), Type II ($\delta = 0°$), and Type III ($\delta = 10°$) have thrust force values of 20.035 N, 18.24 N, and 14.765 N, respectively. Thus, the thrust force is significantly reduced with the raise of the axial rake angle. The curve of average drilling force changing with micro-hole number is presented in Fig. 16, from which it is evident that the drilling force rises linearly as the increase of micro-hole number. Furthermore, it is observed that Type III ($\delta = 10°$) attains the minimum thrust force as compared with Type I ($\delta = -10°$) and Type II ($\delta = 0°$). When machining to the 30th hole, the drilling force values of Type I ($\delta = -10°$), Type II ($\delta = 0°$), and Type III ($\delta = 10°$) are 19.752 N, 19.06 N, and 13.706 N, respectively, and the drilling force of Type III ($\delta = 10°$) is respectively reduced by 30.61% and 28.1% as compared to Type I ($\delta = -10°$) and Type II ($\delta = 0°$). As the axial rank angle raises, the dynamic rake angle γ_{oe} along the inner cutting edge increases while chip deformation is reduced, bringing about a decrease in the thrust force.

5.2 Tool wear

Micro-drilling tests were carried out under the feed rate f of 28 mm/min using three kinds of helical point micro-drills with different axial rake angles. After drilling 30 holes, the micro-drills were cleaned by the ultrasonic cleaner to dislodge the debris such as chips attached to the tool surface. Then the wear profiles of drill bit were observed and measured by a 3D laser scanning microscope, as presented in Fig. 17. The wear of the cutting edge and chisel edge are apparent on all micro-drills. Type II ($\delta = 0°$) exhibits the least tool wear as compared to Type I ($\delta = -10°$) and Type III ($\delta = 10°$). Moreover, the chip adhesion occurs on the flank of Type I ($\delta = -10°$).

The wear band width of the micro-drill tip was measured to conduct the quantitative analysis of tool wear degree, and the measurement method is presented in Fig. 18. Figure 19 shows the maximum wear width values of the cutting edge (VB_{max}) and the chisel edge (C_{max}) of the three tools. It can be observed

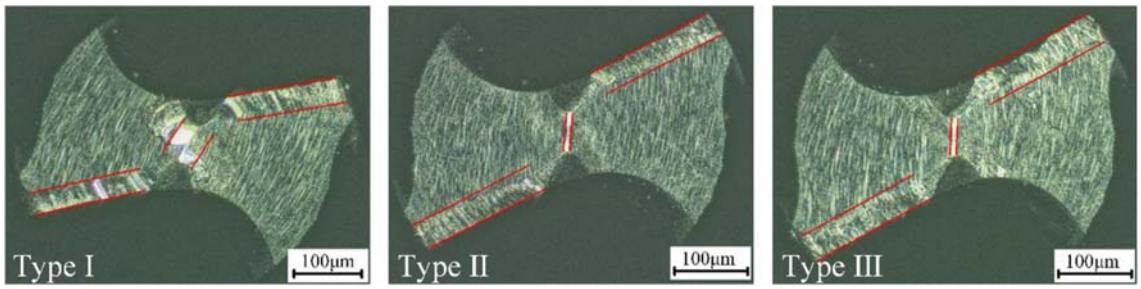

Fig. 17 Microscope photograph of helical point micro-drills with unequal axial rake angles

that the C_{max} and VB_{max} values of Type II ($\delta = 0°$) are the smallest. The C_{max} and VB_{max} values of Type III ($\delta = 10°$) are slightly greater than those of Type II ($\delta = 0°$). Compared with Type I ($\delta = -10°$) and Type III ($\delta = 10°$), the maximum wear width of the chisel edge of Type II ($\delta = 0°$) is respectively reduced by 82.43% and 19.69%, and the maximum wear width of the main cutting edge is respectively reduced by 3.22% and 11.72%. Although the thrust force generated by Type III ($\delta = 10°$) is less than that generated by Type II ($\delta = 0°$), the rake angle along the inner cutting edge of Type III ($\delta = 10°$) is larger than that of Type II ($\delta = 0°$); thus, the inner cutting edge is sharper and easily broken. On the other hand, Type III ($\delta = 10°$) produces the smallest angle between the axes of tool and chip, so the chips slide along the micro-drill rake face over a long range and can easily wrap around the drill. The torque generated by Type III ($\delta = 10°$) is larger than that generated by Type II ($\delta = 0°$) according to the simulation results, which also accelerates the wear and breaking of Type III ($\delta = 10°$). The C_{max} value of Type I ($\delta = -10°$) is significantly larger than that of Type II ($\delta = 0°$), and the VB_{max} value of Type I ($\delta = -10°$) is slightly larger than that of Type II ($\delta = 0°$). The workpiece material adheres to the flank of Type I ($\delta = -10°$), so the C_{max} value of Type I ($\delta = -10°$) is significantly larger than those of Type II ($\delta = 0°$) and Type III ($\delta = 10°$). The thrust force of Type I ($\delta = -10°$) is larger than that of the other tools, so its cutting heat is also the highest; this increases the possibility of tool bonding materials.

5.3 Micro-hole machining quality

The entrance morphology of micro-holes processed by Type I ($\delta = -10°$), Type II ($\delta = 0°$), and Type III ($\delta = 10°$) under the feed rate f of 28 mm/min is presented in Fig. 20. It can be seen that the shape precision of the micro-hole entrance is getting worse with the rise of the micro-hole number. Micro-holes drilled by Type I ($\delta = -10°$) display good micro-hole machining quality before the 18th hole, and significant burrs and breakages at the entrances from the 18th to the 30th holes. Micro-holes drilled by Type II ($\delta = 0°$) have good hole machining quality before the 27th hole, and significant burrs at the micro-holes entrance from the 27th to the 30th holes. Micro-holes drilled by Type III ($\delta = 10°$) display good hole machining quality before the 13th hole, and significant burrs at the entrances from the 13th to the 30th holes. Therefore, the micro-holes drilled by Type II ($\delta = 0°$) have better entrance morphologies compared with those drilled by Type I ($\delta = -10°$) and Type III ($\delta = 10°$).

To quantitatively analyze the micro-hole machining quality, the micro-hole roundness was measured through the measurement method described as Fig. 21. The roundness error is defined as the difference between the incircle radius R_1 and the circumcircle radius R_2. The roundness values of the micro-holes machined by Type I ($\delta = -10°$), Type II ($\delta = 0°$), and Type III ($\delta = 10°$) are presented in Fig. 22, from which it is evident that the roundness is

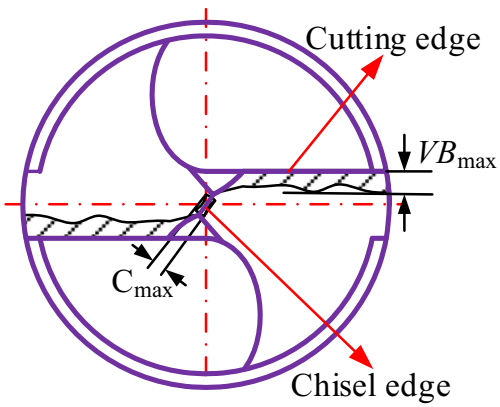

Fig. 18 Measurement method of wear band width

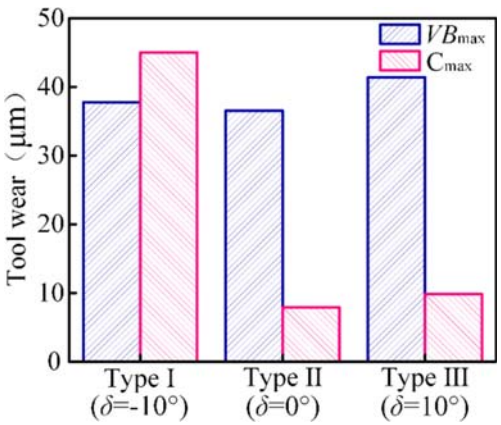

Fig. 19 Measurement results of micro-drill wear

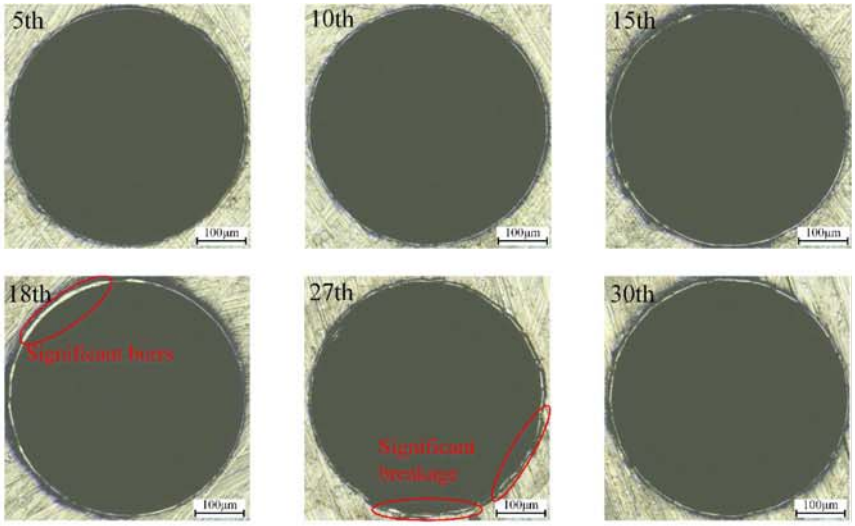

(a) Partial micro-holes machined with Type I (δ = -10°)

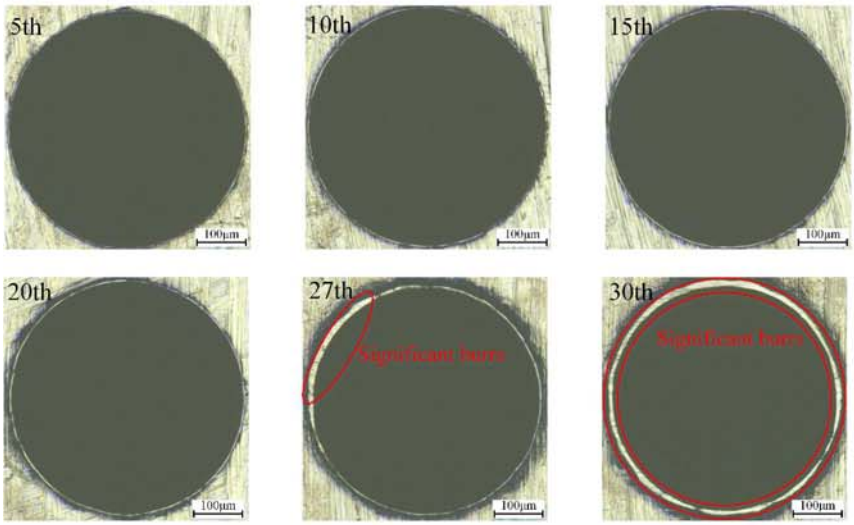

(b) Partial micro-holes machined with Type II (δ = 0°)

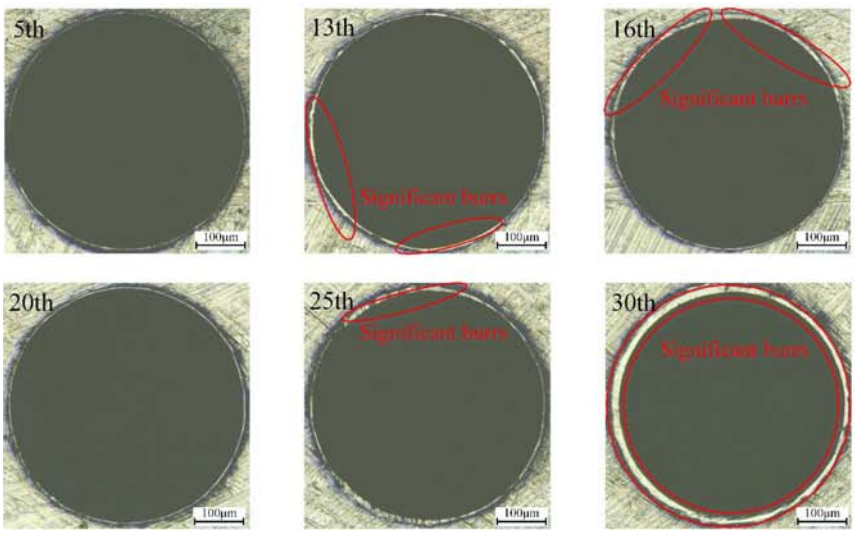

(c) Partial micro-holes machined with Type III (δ = 10°)

Fig. 20 Micro-hole entrance topography produced by the micro-drills with unequal axial rake angles

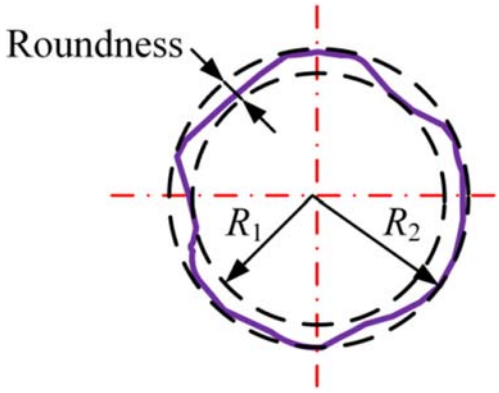

Fig. 21 Measurement method of roundness error

found to increase with the rise of the number of micro-holes. It can be observed from Fig. 22 that the micro-holes processed by Type II ($\delta = 0°$) have the minimum roundness as compared with Type I ($\delta = -10°$) and Type III ($\delta = 10°$). The roundness of the micro-holes drilled by Type III ($\delta = 10°$) is slightly larger than that of the micro-holes machined by Type II ($\delta = 0°$) due to the larger tool wear. The roundness of micro-holes drilled by Type I ($\delta = -10°$) has small values before the 10th hole, and significantly increases from the 11th to the 30th holes due to the flank bonding materials of the Type I ($\delta = -10°$). When drilling to the 30th hole, Type I ($\delta = -10°$), Type II ($\delta = 0°$), and Type III ($\delta = 10°$) result in roundness values of 6.49 μm, 4.757 μm, and 5.365 μm, respectively. Compared with Type I ($\delta = -10°$) and Type III ($\delta = 10°$), the micro-hole roundness error of Type II ($\delta = 0°$) respectively decreases by 26.7% and 11.33%.

With respect to chip morphology, the angle between the axes of tool and chip gradually comes down with the rise of the axial rake angle, and the chips are then prone to wrap around the drill. The thrust force is significantly reduced, but the torque increases with the rise of the axial rake angle. As for the drill tip wear and micro-hole processing quality, the micro-drills with a 0° axial rake angle have the minimum tool wear, and the micro-holes drilled by this micro-drill display better micro-hole quality. The thrust force for the micro-drills with a − 10° axial rake angle is the largest, which results in greater tool wear and poorer micro-hole quality. The larger torque and lower rigidity of the inner cutting edge of the micro-drills with the 10° axial rake angle lead to poorer drilling performance. Thus, helical point micro-drills having the 0° chisel edge axial rake angle are suitable for drilling 304 austenitic stainless steel.

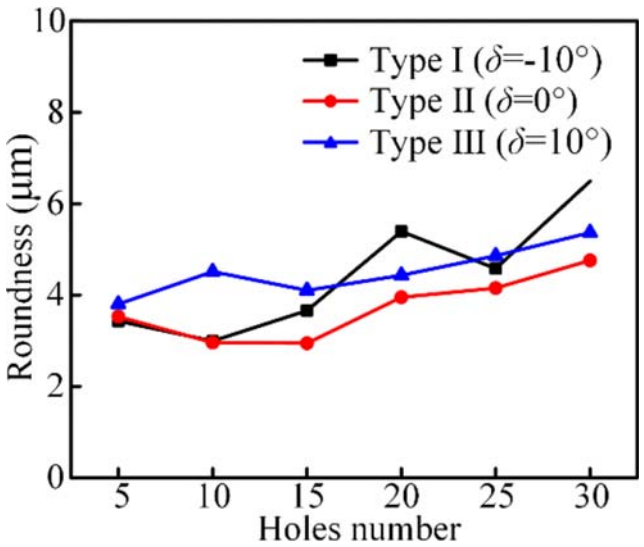

Fig. 22 Change of roundness value with the micro-hole number

6 Conclusions

In this paper, through finite element simulations and micro-drilling experiments, the effect of the axial rake angle by the thinning of the chisel edge on the machining performance of micro-drills was investigated, and the main conclusions below can be drawn.

(1) With the rise of the chisel edge axial rake angle, the chip deformation degree and thrust force decrease owing to the increase of the rake angle along the inner cutting edge; besides, the angle formed between tool axis and chip axis gradually decreases owing to the reduction of the rake angle gradient along the cutting edge; finally, the thickness and width of the uncut chip of the inner cutting edge increase, bringing about a rise in the torque.

(2) The smallest tool wear of micro-drills having a 0° axial rake angle is obtained due to their medium thrust force and torque; they also result in better micro-hole entrance morphology and minimum roundness. When drilling to the 30th hole, compared with Type I ($\delta = -10°$) and Type III ($\delta = 10°$), the chisel edge maximum wear width of Type II ($\delta = 0°$) is respectively reduced by 82.43% and 19.69%, and the micro-hole roundness respectively decreases by 26.7% and 11.33%. The thrust force for the micro-drills with a − 10° axial rake angle is the largest, so it causes the larger drill tip wear and poorer micro-hole processing quality. The larger torque and lower rigidity of the inner cutting edge of the micro-drills having a 10° axial rake angle lead to poorer drilling performance.

Funding information The research received the financial support of the National Key R&D Program of China under Grant No. 2019YFB1311100, the National Natural Science Foundation of China under Grant No. 51975053, and the Basic Research Program under Grant No. DEDPHF and Grant No. DEDPYDJ.

References

1. Chyan HC, Ehmann KF (1998) Development of curved helical micro-drill point technology for micro-hole drilling. Mechatronics 8(4):337–358
2. Yan L, Jiang F (2013) A practical optimization design of helical geometry drill point and its grinding process. Int J Adv Manuf Technol 64(9–12):1387–1394
3. Zhang SY, Liang ZQ, Wang XB, Zhou TF, Jiao L, Yan P, Jian HC (2016) Grinding process of helical micro-drill using a six-axis CNC grinding machine and its fundamental drilling performance. Int J Adv Manuf Technol 86(9–12):2823–2835
4. Karsten M, Vuuren BJV, Barnaud A, Terblanche JS (2014) Finite element investigation and optimization of tool wear in drilling process of difficult-to-cut nickel base superalloy using response surface methodology. Int J Adv Des Manuf Technol 8(1):446–446
5. Zheng LJ, Wang CY, Fu LY, Yang LP, Qu YP, Song YX (2012) Wear mechanisms of micro-drills during dry high speed drilling of PCB. J Mater Process Technol 212(10):1989–1997
6. Kudla LA (2011) Fracture phenomena of microdrills in static and dynamic conditions. Eng Fract Mech 78(1):1–12
7. Guo HX, Wang XB, Liang ZQ, Zhou TF, Jiao L, Liu ZB, Teng LL, Shen WH (2018) Drilling performance of non-coaxial helical flank micro-drill with cross-shaped chisel edge. Int J Adv Manuf Technol 99(5–8):1301–1311
8. Guo HX, Liang ZQ, Wang XB, Zhou TF, Jiao L, Teng LL, Shen WH (2018) Influence of chisel edge thinning on helical point micro-drilling performance. Int J Adv Manuf Technol 99(9–12): 2863–2875
9. Nanbu Y, Ochiai K, Ehara K, Matsuda S (2010) High-aspect-ratio microdrilling of the nozzle for gas turbine (2nd report): effect of thinning of microdrill and ultrasonic vibration. Proceedings of JSPE Semestrial Meeting (J Jpn Soc Precis Eng) 2010:1017-1018
10. Nanbu Y, Ochiai K, Horio K, Kaneko J, Watanabe T, Matsuda S (2011) Influence on rake angle of chisel edge in high-aspect-ratio microdrilling. J Jpn Soc Precis Eng 77:713–717
11. Xiang WJ, Zhou ZX, Hu SJ, Yang J, Liang JP (2006) Mathematical model and simulation of regrind chisel edge for helical micro-drill. Key Eng Mater 304-305:550–554
12. Wang X, Zheng XH, An QL, Chen M (2012) Experimental investigation on drilling pcb through-holes. Adv Mater Res 426:56–59
13. Lin PD, Tzeng CS (2007) New method for determination of the pose of the grinding wheel for thinning drill points. Int J Mach Tools Manuf 47(15):2218–2229
14. Lin C, Kang SK, Ehmann KF (1995) Helical micro-drill point design and grinding. J Eng Ind 117(3):277
15. Kang SK, Lin C, Ehmann KF (1993) Comparative analysis of planar and helical micro-drill points. Trans NAMRI/SME XXI:189–196
16. Fischer CE, Wu WT, Chigurupati P, Jinn JT, Ghosh S, Castro JC, Lee JK (2004) Application of three dimensional finite element modeling for the simulation of machining processes. AIP Conf Proc 712:1353–1358
17. Oden JT (2004) Finite element method. Dictionary Geotechnical Engineering/wörterbuch Geotechnik 73(4Suppl1):3–13
18. Danish M, Ginta TL, Habib K, Rani AMA, Saha BB (2019) Effect of cryogenic cooling on the heat transfer during turning of AZ31C magnesium alloy. Heat Transfer Eng 40(12):1023–1032
19. Abouridouane M, Klocke F, Lung D (2013) Microstructure-based 3D finite element model for micro drilling carbon steels. Procedia CIRP 8:94–99
20. Ekrem O, Stefan H, Dirk B (2019) Development of a three-dimensional finite element method simulation model to predict modified flow drilling tool performance. Int J Mater Form 12(3): 477–490
21. Liang ZQ, Jian HC, Wang XB, Zhao WX, Zhang SY, Otani Y, Xue SY (2014) A 5-Axis coordinated CNC grinding method for the flank of a non-coaxial helical micro-drill with the cylinder grinding wheel. Adv Mater Res 1017:654–659
22. Zhang SY, Wang XB, Liang ZQ, Zhou TF, Jiao L, Yan P (2017) Modeling and optimization of the flute profile of micro-drill. Int J Adv Manuf Technol 92(5–8):2939–2952